Molecular Interactions Balanced One- and Two-Dimensional Hybrid Nanoarchitectures for High-Performance Supercapacitors

*Mingxia Lu[a], Gang Wang[a], Bo Li[a], Jing Chen[a], Jingchao Zhang[b], Zhe Li[c] and Bo Hou[d,]**

[a] College of Chemistry, Chemical and Environmental Engineering, Henan University of Technology, Zhengzhou 450001, P. R. China.

[b] Holland Computing Center, University of Nebraska-Lincoln, Lincoln, NE, 68588, USA

[c] School of Engineering, Cardiff University, Cardiff, CF24 3AA, UK

[d] Engineering Department, University of Cambridge, 9 JJ Thomson Avenue, Cambridge CB3 0FA, UK University of Cambridge, CB3 0FA, Cambridge, UK

* Corresponding author. Tel: +44 (0)1223 748318. Email: bh478@cam.ac.uk (Bo Hou)

Abstract:

Hybridising one-dimensional (1D) and two-dimensional (2D) materials to enhance charge storage have received considerable attention, but fundamental understandings of inherent ratio-dependent charge transfer mechanisms associated with the modulation of their molecule interactions still lacks within the community. Herein, we exemplified through 1D surface oxidised carbon nanotubes (Ox-CNTs), and 2D reduced graphene oxide (rGO) to understand their ratio-dependent charge transfer and molecule interaction dynamics. We found stepwise ultrasonication and self-assembly process can control the thermodynamic molecular interactions, which result in rGO, Ox-CNT suspensions not only well dispersed in N, N-dimethylformamide but also self-organised into sandwiched nanoarchitectures. We unravel that the enhanced charge storage performance is originated from the Ox-CNT-mediated low contact resistance between the active material and the current collector, and the incorporation of rGO leads to a significant ion diffusion coefficient and gives rises to numerous ion diffusion channels for high rate retention. Through a systematic electrochemical characterisation, we found the GC5:5 hybrids (mass ratio of rGO to Ox-CNT) provide the best compromise-balance ratio between rGO and Ox-CNT for realising champion energy density (9 $Wh \cdot kg^{-1}$) and power density (10 $kW \cdot kg^{-1}$) beyond the state-of-the-art performance from their individuals. Our results herald the advent of molecular level hybridisation of 1D-2D materials for high-performance electrochemical energy storage.

Keywords: reduced graphene oxide (rGO), carbon nanotubes (CNTs), charge storage, hybridisation, 2D material

Introduction

Electrochemical double-layer capacitors (EDLCs) are prevalent supercapacitors that are formed by a sandwich structure which contains two conductive plates surrounding a dielectric or insulator.[1-3] EDLCs store energy using ion adsorption instead of the redox reaction which has been primarily considered as a crucial electrical energy storage technology for electric vehicles (EVs), hybrid electric vehicles (HEVs), portable electronics, and others[4-6]. However, further enhancement of energy density in the recent development of EDLCs is gradually becoming difficult, owing to grand challenges in discovering new materials.[7-9] In principle, the capacitance and charge-discharge rates of EDLCs scale with surface area and electrical conductivity. Therefore, as far as electrodes can have i) a large electrochemically active specific surface area, ii) continuous channels for ion transport with appropriate pore size distribution, iii) high electrical conductivity, and good wettability[6, 10], considerable performance enhancement can be achieved from rationally designed material structures.[1, 11]

Low-dimensional carbon-based nanomaterials are the most promising and well-established one-dimensional (1D) and two-dimensional (2D) candidates for high-performance supercapacitors associated with their earth-abundant and non-toxic natures[11, 12]. Besides of graphene, 2D reduced graphene oxide (rGO) has been proposed as an electrode material for supercapacitor, and it exhibited an excellent specific capacitance of 117 $F \cdot g^{-1}$ in 1 M H_2SO_4 aqueous solution[13]. However, the rGO-based supercapacitors cannot be used in high current applications because their specific capacitance dramatically decreased when increasing the current density[14]. The main challenges for the rGO-based supercapacitors are i) rGO is very easy to form irreversible agglomerates caused by strong van der Waals interaction between rGO sheets during the drying process[15, 16]; ii) rGO has an electrical conductivity of about 100 $S \cdot m^{-1}$, which is much lower than the other carbon-based candidates such as single-walled carbon nanotubes (about 10000 $S \cdot m^{-1}$)[17]. Therefore, introducing spacers between rGO sheets to prevent

their re-stacking is considered to be a viable solution to address this challenge [18, 19].

1D carbon nanotubes have been reported as effective spacers between 2D graphene sheets to improve capacitance owing to their high electrical conductivity, excellent mechanical strength, and proprietary hollow structure[20-25]. For instance, the graphene/multiwall carbon nanotubes (GR/MWCNT) hybrid electrode has been demonstrated to have enhanced specific capacitance of 91 $F \cdot g^{-1}$ in 1 M Na_2SO_4 aqueous solution, which is much higher than pure GR and pure MCNT[21]. Recently, rGO/single-wall carbon nanotube (rGO/CNT) hybrid film has also been fabricated and shown much higher specific capacitance (132 $F \cdot g^{-1}$) than GR/MCNT[22]. Even though graphene/CNT hybrid materials have been studied in improving the performance of supercapacitors, rGO/CNT-based supercapacitors and their ratio-dependent electrochemical performance are still lacking within the community.

Herein, we use stepwise ultrasonication and self-assembly process to realise superior controllability between disequilibrium and equilibrium thermodynamic molecular interactions, which result in rGO/Ox-CNT suspension not only well dispersed in N, N-dimethylformamide (DMF) but also self-organised into unique sandwiched nanoarchitectures. Based on electron microscopy analysis, we found the intercalation of CNT into the rGO sheets can form a rich porous structure, which provides open channels for ion transport and reduces ion diffusion resistance. Also, the electrochemical impedance spectroscopy (EIS) studies show that the addition of CNT can dramatically improve the electrical conductivity of rGO and enable a high charge transfer rate. In the end, we successfully show a champion energy density from GC5:5 hybrids (mass ratio of rGO to Ox-CNT was 5:5) and demonstrate the potential of rGO/CNT as promising electrode materials with high energy density and power density.

Experimental section

Preparation of GO and rGO

The growth of GO. A modified Hummers approach was employed for the preparation of graphene oxide from natural graphite (Graphite was purchased from Aladdin Industrial

Corporation with 1200 mesh, purity > 99.95%). Typically, 1.5 g of graphite was added into a flask with 180 mL of concentrated H_2SO_4 and 20 mL of H_3PO_4 at room temperature. 9.0 g of $KMnO_4$ powder was gradually added into the graphite suspension solution under vigorous stirring to keep the temperature around at 30 ℃. The temperature of the solution was subsequently raised to 50 °C for a 12 h reflux reaction, and the reaction was quenched by an ice bath together with the swift injection of 200 mL ice water. Furthermore, 30% H_2O_2 was dropwise added to remove $KMnO_4$, and the colour of suspension was changed from purple-black to bright yellow. The mixture was centrifuged and washed with 10% HCl aqueous solution to remove metal ions, followed by repeated centrifugation and washing with distilled water until the pH of the solution reached around 5. In the end, the resulting GO solid was dried at 80 °C for two days.

The growth of rGO. 100 mg of as-prepared GO was dispersed into 200 mL of NaOH aqueous solution (pH =11) under ultrasonication (1 h), followed by adding 0.2 mL of hydrazine hydrate. The mixture was stirred and reflux at 90°C for 2 h reduction reaction. Then the resulting product was recovered by filtration and washed with distilled water and acetone for 5 times. In the end, the rGO powder was obtained by drying at 80 ℃ for 24 h.

Preparation of Ox-CNT

200 mg of single-walled carbon nanotubes (SWCNTs, purity > 95%, diameter: 1~2 nm, length: 5~30 μm, Nanjing XFNANO Materials Tech Co., Ltd) were dispersed into 80 mL H_2SO_4 and HNO_3 mixture (3:1 v/v) in a 250 mL beaker. After sonication for 4 h at room temperature, the mixture was then diluted by slowing adding of 200 mL of distilled water. Later, the resulting product was recovered from the solution by filtration and washed with distilled water and acetone several times. In the end, the Ox-CNT was collected by drying at 80 °C for 48 h.

Preparation of rGO/Ox-CNT and GO/ Ox-CNT electrodes

A 0.5 $mg{\cdot}mL^{-1}$ rGO and Ox-CNT suspensions were prepared by dispersing rGO or Ox-CNT powders into DMF under continuous sonication (KQ-300VDE, 45 kHz, 48 h). Different ratios of rGo/Ox-CNT solution was prepared by mixing Ox-CNT dispersion with rGO dispersion

under a weight ratio of 5:1, 5:3, and 5:5, respectively. After mixing, the solutions were sonicated for 2 hours and leave the solution standstill overnight for the self-assembly process. The solids were filtrated by a microporous membrane (0.22 μm) and dried at 80 ℃ overnight. Each mixture was denoted as GC5:1, GC5:3 and GC5:5, respectively.

The as-prepared rGO, Ox-CNT, and mixture were mixed with carbon black and PVDF into N-methyl-2-pyrrolidone (NMP) solvent, to form homogeneous slurry with a weight ratio of 8:1:1. This slurry was coated onto the nickel foam substrate (1×2 cm), dried at 80 ℃ for 12 h, and then pressed at a pressure of 10 MPa to form a thin sheet using as working electrode.

The preparation of GO, Ox-CNT and mixture electrodes were followed the same procedures as rGo/Ox-CNT hybrids. Each mixture was denoted as GOC25:2, GOC5:2 and GOC3:2.

Characterisation

The microstructure and morphology were analysed by an FEI-Quanta 250 FEG scanning electron microscopy (SEM, FEI, Hillsboro, USA) with 10 kV operating voltage. X-ray diffraction (XRD) patterns were collected on Rigaku MiniFlex 600 X-ray diffractometer (Rigaku Co., Tokyo, Japan) with Cu Kα radiation over the 2θ range of 5°−80°. Raman spectrometer was carried out on a dried solid with an excitation wavelength of 532 nm (LabRAM HR Evolution, HORIBA Jobin Yvon, France). Fourier transform infrared spectrum of all the samples were recorded on a Nicolet Avatar 360 FT-IR spectroscopy (FT-IR, Instrument Co., Madison, WI, USA).

Electrochemical measurements

All the electrochemical measurements including cyclic voltammetry (CV), electrochemical impedance spectroscopy (EIS) and galvanostatic charge-discharge (GCD) were performed on a CHI660E electrochemical workstation (Shanghai Chen Hua Instruments Co., Shanghai, China) in a three-electrode cell. Three electrodes in a one-compartment cell consisted of the as-prepared carbon material electrode as the working electrode, a Pt sheet (2 cm × 2 cm) as the counter electrode, Ag/AgCl (saturated KCl) as the reference electrode, and 1 M $NaSO_4$ aqueous

solution as the electrolyte. The CV curves were acquired in a potential range of 0-1 V at a scan rate of 10 mV·s^{-1}. EIS measurements were measured in a frequency range from 10^{-2}-10^{5} Hz with an ac amplitude of 5 mV at open circuit potential. GCD tests were performed at a current of 5, 10, 20, 50 mA.

The gravimetric specific capacitances (C_s) were calculated from the GCD discharge curves using the following equation

$$C_s = \frac{I \cdot \Delta t}{m \cdot \Delta U} \qquad (1)$$

where I is the current (A), Δt is the discharge time (s), and ΔU (V) is the potential range after the IR drop is removed.

The gravimetric energy density (Wh·kg^{-1}) of each device was calculated using

$$E = \frac{C_s \cdot \Delta U^2}{2 \times 3600} \qquad (2)$$

The gravimetric power density (W·kg^{-1}) of the device was calculated from

$$P = \frac{E}{\Delta t} \times 3600 \qquad (3)$$

Results and discussion

We fabricate the GO/CNT and the rGO/CNT hybrids through an ultrasonication and self-assembly process which enable a right balance between disequilibrium and equilibrium thermodynamic molecular interactions.[26, 27] As shown in Scheme 1, the CNT and GO were well dispersed in DMF via continuous ultrasonication treatment and these sonication processes enable disequilibrium thermodynamic molecular interactions, which result in CNT and GO well dispersed and mixed in DMF. Then, the solution was standstill overnight for thermodynamic equilibrium molecular self-assembly process where CNT and GO stacked into sandwich structure associated with the van der Waals force.[22, 26] Figure 1 shows the microstructure and morphologies of Ox-CNT, GO, rGO, and rGO/CNT hybrids through SEM analysis. Typical

Ox-CNT network formed by random stacking of dispersed carbon nanotubes can be resolved in Figure 1(a). Figure 1(b) and Figure 1(c) show the multi-layered morphologies of GO and rGO which were formed by multi-stacking of GO (or rGO) sheets driven by van der Waals force[22]. In Figure 1(d~e), the cross-section SEM images reveal that the rGO/CNT hybrids have an interconnected porous structure. As highlighted in Figure 1(g-i) and Figure S1, these aligned Ox-CNTs intercalated into rGO layers not only suppress the further-accumulation of rGO stacking sheets but also provide good porosity in the hybrid associated with the maximum utilisation of Ox-CNT.[26, 27]

The localised crystal structure from as-prepared GO, rGO, and rGO/CNT hybrids were determined via XRD analysis. Figure 2(a) shows the XRD patterns of natural graphite (Gt), GO, and rGO. A typical interlayer diffraction peak (i.e., $2\theta = 9.8°$) was observed which corresponds to a *ca.* 0.90 nm interlayer spacing between each GO sheets. Compared to the characteristic peak (002) of Gt ($2\theta = 26.4°$, d = 0.34 nm), the interlayer spacing of GO is largely expanded. It indicates that the introduction of oxygen moieties can effectively functionalise and separate the GO sheets.[27] After the reduction reaction, the interlayer spacing peak ($2\theta=9.8°$) was decreased, and a broad peak at 24.5° (d = 0.36 nm) emerged. As shown in Figure 2(b), the decrease of interlayer distance suggest that GO was successfully reduced, and the broader peaks indicated high stacking disorder[22] which means the depletion of oxygen in rGO and rGO/Ox-CNT hybrid samples.

FT-IR analysis was performed to further investigate the chemical structure of GO, rGO, Ox-CNT, and rGO/Ox-CNT hybrids as a function of their mass ratios (5:1, 5:3, and 5:5). As shown in Figure 3(a), the FTIR spectrum of Ox-CNT shows a series of characteristic peaks at around 3420, 3140, 1630, 1400, and 1120 cm^{-1}. Usually, the absorption peak at 3420 cm^{-1} and 1630 cm^{-1} are attributed to O−H hydroxyl stretching vibrations and bending vibrations of adsorbed water molecules. The absorption peak at 3140, 1400, and 1120 cm^{-1} are assigned to O−H carboxyl stretching vibration, O−H hydroxyl deformation vibration, and C–OH stretching vibration, respectively. Compare to the Ox-CNT, GO shows much weaker signals in 1700-1775 cm^{-1} (C=O carbonyl stretching vibration), 1550 cm^{-1} (C=C stretching vibration of benzene

ring), 1225 cm^{-1} (C−O epoxy stretching vibration), 1020 cm^{-1} (C−O alkoxy stretching vibration), and 680-880 cm^{-1} (C−H out-of-plane bending vibration of aromatic ring). In addition, the spectra baseline of GO is indistinguishable from its characteristic FTIR peaks, which indicates the oxidation process occurs not only on edge but also on the graphite layers. Moreover, the typical absorption bands from oxygen-containing groups such as carboxyl and hydroxyl moieties, as well as a small amount of alkoxy group and epoxy group (C=O, C−H, and C−O) dramatically decreased in rGO and rGO/Ox-CNT samples,[28-32] which indicate the successful reduction of GO.

The typical Raman spectra of GO, rGO, Ox-CNT, and rGO/Ox-CNT hybrids are shown in Figure 3(b) (see full-spectrum in Figure S2). The D-band at around 1340 cm^{-1} is attributed to the defect or disorder structure, and the G-band at about 1590 cm^{-1} is corresponding to the vibration of sp^2 hybrid carbon atoms.[33, 34] In general, the peak intensity ratio of D-band and G-band (I_D/I_G) can provide a sensitive metric for the disorder degree in sp^2 carbon materials. Typically, 1.14 for GO, 1.09 for rGO, 0.018 for GC5:1, 0.034 for GC5:3, 0.074 for GC5:5, and 0.036 for Ox-CNT.[33-35] Therefore, the reduction effect can be determined through the value of I_D/I_G for rGO (1.09) which is smaller than that of GO (1.14). After intercalation of Ox-CNT, the value of I_D/I_G drop dramatically and close to the value of Ox-CNT, which is attributed to the higher peak intensity of Ox-CNT than rGO. Also, this value slightly increases with the increasing of Ox-CNT content (GC5:1 < GC5:3 < GC5:5), indicating that the structure disorder is increased. From Figure 3(c), it can be seen that the 2D-Band peak of GO is weaker than rGO due to the restacking of GO sheets by interlayer hydrogen bonding[36]. The broad peak of 2D-band indicates rGO sheets restack more compact after reduction. In comparison, rGO/Ox-CNT hybrids exhibit a sharp and intense 2D peak, which suggests that the addition of Ox-CNT can effectively prevent the molecule interactions between each rGO sheets.

To understand charge storage and transfer dynamics of CNT as a function of their surface redox treatment, cyclic voltammetry (CV), electrochemical impedance spectroscopy (EIS) and galvanostatic charge/discharge (GCD) analysis were performed successively on as-prepared supercapacitors. As shown in Figure 4(a), CNT and Ox-CNT show characteristic rectangular

CV curves resulting from the formation of electrochemical double-layer capacitance by fast charge transfer and electrolyte diffusion with negligible Faradaic reactions. The Ox-CNT electrode shows a larger integral area than CNT electrode, which indicates a higher specific capacitance. This phenomenon is attributed to the increased specific surface area of CNT after the acid oxidation treatment, which also contributes to the fast charge transfer as observed in the EIS analysis (Figure 4b). The Nyquist plots are fitted with a typical equivalent circuit (inset) for extracting charge transfer (i.e., high-frequency semicircles) and ion diffusion (i.e., low-frequency straight lines) parameters.[9] As highlighted in Figure 4(c), Ox-CNT electrode shows a smaller diameter of the semicircle compared to CNT which indicates that the presence of the oxygen-containing groups can facilitate the charge transfer between the electrode and electrolyte[9, 37].

Furthermore, the straight-line part in Ox-CNT medium-frequency EIS shows a steeper slope than CNT, which means a smaller Warburg impedance and better ion diffusion can be obtained after acid oxidation treatment on CNT. In Figure 4 (d), the GCD curve (e.g., 1.25 A/g) of the Ox-CNT shows longer GCD time and symmetric linearity. Under the same electrochemical conditions, the longer GCD time of the Ox-CNT electrodes means a higher charge storage capacity, which can be attributed to the enlarged specific surface area and abundant oxygen-containing groups. Indeed, as calculated from equation (1), the specific capacitance of Ox-CNT electrode is 25 F/g, which is higher than the CNT electrode (15 F/g).

Moreover, we performed frequency-dependent capacitance analysis through EIS Bode phase plots (Figure 4 e and f) with a frequency range from 10^{-2}-10^{5} Hz. Although supercapacitors usually lose their dc-rated capacitance at high frequencies (and therefore their energy storage capability), we found that the Ox-CNT sample still exists considerable high capacitance compared to CNT. The relative slow capacitance and the series resistance drop indicate Ox-CNT can offer less ionic resistance and better ion pathway to meet the high-frequency response.

The as-prepared GO, and rGO-based supercapacitors were also characterised electrochemically to understand their charge storage and ion transfer properties. As shown in Figure 5 (a), the rGO

electrode exhibits a much higher specific capacitance than GO electrode. This phenomenon is attributed to the changing of band gap as well as an increased specific surface area of rGO after the reduction treatment. The Nyquist EIS plots were fitted with an equivalent circuit (inset) for extracting charge transfer and ion diffusion parameters. As shown in the EIS Nyquist plots (Figure 5b and Figure 5c), a small semicircle together with a steeper liner region are present in the rGO electrode which indicates the rGO has a smaller Warburg impedance as well as high capacitance compared to GO. In Figure 5 (d), the GCD curve of the rGO shows longer GCD time and symmetric linearity, which further confirmed that the rGO electrodes have a higher charge storage capacity. Indeed, as demonstrated in the EIS Bode phase plots (Figure 5 e and f), the rGO exists high capacitive behaviour compared to GO. In particular, a prolonged reduction treatment (Figure 5f) could further boost the potential dependent capacitance as well as alleviate the capacitance and the series resistance degeneration with the frequency. It indicates that rGO can offer a better high-frequency response associated with their high ion and charge conductivity.

The enhanced charge storage and charge transfer performance as a function of the rGO/Ox-CNT hybridisation ratio are demonstrated in Figure 6. It can be seen from the CV plots (Figure 6a and Figure S3) that the specific capacitance of all rGO/Ox-CNT hybrids exhibits an overall higher performance than pure Ox-CNTs, which attributes to the rGO-mediated high specific surface area and fast ion transfer. Furthermore, the specific capacitance of rGO/Ox-CNT hybrids are monotonically decreasing with rGO loading, indicates a decrease in electrical conductivity. On the other hand, the addition of Ox-CNT can improve electric conductivity and reduce the internal resistance of rGO. The enhanced charge transfer performance could be revealed from the Nyquist EIS plots (Figure 6b), where the intersection of semicircle from GC5:5 combinations (~2.25Ω) are much smaller than the other samples. The Warburg impedance of GC5:5 is also decreased as confirmed from the more steeper liner region. It indicates a low rGO loading could enable a smaller Warburg impedance as well as high capacitance compared to pure Ox-CNT. In Figure 6 (c and d), the EIS Bode plots of the GC5:5 sample shows considerable high capacitive behaviour compared to the others at lower frequency range.

To better understand the frequency response of the electrode, the relaxation time constant t_0 was calculated, as shown in Figure 6(d). Generally, t_0 represents the minimum time required to discharge the stored energy with 50% efficiency[38]. Compare with the other rGO/Ox-CNT hybrids and rGO, GC5:5 exhibited the smallest t_0 of 6.8 s, indicating the fastest response to charge-discharge characteristics and the most facile penetration of ions into pores. It should be noted that this significant charge storage and transfer enhancement cannot be realised in the case of GO/Ox-CNT samples (Figure 6e to Figure 6h). Compared to rGO, the addition of GO into Ox-CNT (Figure 6e to Figure 6h) will decrease the capacitance and suppress the charge transfer, which is due to the poor charge and ion conductivity from GO.

In Figure 7a, we rationalised the supercapacitor performance of rGO/Ox-CNT hybrid as a function of mixing ratio through GCD plots. The CV curves and GCD curves of GC5:5 with different scan rate and current density are also provided in Figure S4 a and b. It can be seen that GC5:5 ratio rGO/Ox-CNT mixture exhibited a symmetric and triangular shape with extended charging and discharging time, which further confirmed the rGO/CNT (5:5) electrodes have the highest specific capacitance and relatively small "IR drop" as compared to other combinations. The calculated specific capacitance values from all electrodes were summarised in Figure 7b. It can be seen that rGO/Ox-CNT electrodes exhibit much higher rate capability than pure Ox-CNT or rGO under the same current densities. The rGO/Ox-CNT electrode also shows better capacity retention compared to rGO and Ox-CNT with 76% capacity retention when increasing the current density from 0.5 to 10 $A \cdot g^{-1}$. The derived Ragone plots in Figure 7c shows the relationship between energy density and power density as a function of rGO/Ox-CNT ratios. Encouragingly, an energy density of 9 $Wh \cdot kg^{-1}$ and a power density of 10 $kW \cdot kg^{-1}$ can be successfully achieved from the GC5:5 hybridised rGO/Ox-CNT electrodes which is higher or comparable to other reported works (Figure S4c).[30, 39-41] Furthermore, as shown in Figure 7d, GC5:5 hybridised rGO/Ox-CNT electrodes exhibit good cycle stability, retaining above 70% after 2000 charge-discharge cycles at a current density of $1A \cdot g^{-1}$.

Conclusions

In conclusion, we have demonstrated excellent electrochemical charge storage and transfer performance based on a ratio-dependent 1D-2D hybrid nanoarchitectures. We found stepwise ultrasonication and self-assembly process can enable a good separation between disequilibrium and equilibrium thermodynamic molecular interactions, which result in rGO/Ox-CNT suspension not only well dispersed in DMF but also self-organised into unique sandwiched nanoarchitectures. We elucidate that the hybridisation of rGO and Ox-CNT could provide excellent charge transfer due to the Ox-CNT mediated low contact resistance between the active material and the current collector. The rGO nanostructure with a high aspect ratio not only leads to a significant diffusion coefficient but also results in a large contact area, which gives rises to numerous ion diffusion channels, thereby inducing high rate retention. Through a systematic electrochemical characterisation on different ratio rGO/Ox-CNT hybridised supercapacitors, we found the GC5:5 provide the best balance ratio between rGO and Ox-CNT for realising both high specific surface area and fast charge transfer. In the end, we demonstrate an energy density of 9 $Wh \cdot kg^{-1}$ and a power density of 10 $kW \cdot kg^{-1}$ can be achieved from the GC5:5 hybridised rGO/Ox-CNT electrodes. The present findings suggest that a rationally designed 1D-2D hybrid nanoarchitecture can have numerous excellent functionalities for the high-performance electrodes in supercapacitors. It also guides the rational structural design based on carbon-based materials which may open new opportunities for batteries, water splitting, and other electrochemical energy storage devices.

Acknowledgements

This work was supported by PhD Programs Foundation of the Henan University of Technology (No. 31401546), Fundamental Research Funds for the Henan Provincial Colleges and Universities, China (No. 2016NQJH06). The Science and Technology Foundation of Henan Province (No. 192102210044, and No. 182102410092).

Supporting Information

See supplementary material for Figure S1 to Figure S4 and Table S1.

References

1. K. Naoi, W. Naoi, S. Aoyagi, J.-i. Miyamoto and T. Kamino, Accounts of Chemical Research, 2013, **46**, 1075-1083.
2. L. L. Zhang and X. S. Zhao, Chemical Society Reviews, 2009, **38**, 2520-2531.
3. S. W. Lee, B. M. Gallant, H. R. Byon, P. T. Hammond and Y. Shao-Horn, Energy & Environmental Science, 2011, **4**, 1972-1985.
4. Y. J. Kim, C.-M. Yang, K. C. Park, K. Kaneko, Y. A. Kim, M. Noguchi, T. Fujino, S. Oyama and M. Endo, ChemSusChem, 2012, **5**, 535-541.
5. R. R. Salunkhe, Y.-H. Lee, K.-H. Chang, J.-M. Li, P. Simon, J. Tang, N. L. Torad, C.-C. Hu and Y. Yamauchi, Chemistry – A European Journal, 2014, **20**, 13838-13852.
6. S. I. Wong, J. Sunarso, B. T. Wong, H. Lin, A. Yu and B. Jia, Journal of Power Sources, 2018, **396**, 182-206.
7. A. S. Aricò, P. Bruce, B. Scrosati, J.-M. Tarascon and W. van Schalkwijk, Nature Materials, 2005, **4**, 366-377.
8. D. Sheberla, J. C. Bachman, J. S. Elias, C.-J. Sun, Y. Shao-Horn and M. Dincă, Nature Materials, 2016, **16**, 220.
9. B. Hou, M. Sohn, Y.-W. Lee, J. Zhang, J. I. Sohn, H. Kim, S. Cha and J. M. Kim, Nano Energy, 2019, **62**, 764-771.
10. J. Yan, Q. Wang, T. Wei and Z. Fan, Advanced Energy Materials, 2014, **4**, 1300816.
11. H. R. Byon, S. W. Lee, S. Chen, P. T. Hammond and Y. Shao-Horn, Carbon, 2011, **49**, 457-467.
12. M. F. El-Kady, V. Strong, S. Dubin and R. B. Kaner, Science, 2012, **335**, 1326-1330.
13. S. R. C. Vivekchand, C. S. Rout, K. S. Subrahmanyam, A. Govindaraj and C. N. R. Rao, Journal of Chemical Sciences, 2008, **120**, 9-13.
14. L. Qiu, X. Yang, X. Gou, W. Yang, Z.-F. Ma, G. G. Wallace and D. Li, Chemistry – A European Journal, 2010, **16**, 10653-10658.
15. J. Chen, C. Li and G. Shi, The Journal of Physical Chemistry Letters, 2013, **4**, 1244-1253.
16. M. D. Stoller, S. Park, Y. Zhu, J. An and R. S. Ruoff, Nano Letters, 2008, **8**, 3498-3502.
17. Q. Cheng, J. Tang, J. Ma, H. Zhang, N. Shinya and L.-C. Qin, Physical Chemistry Chemical Physics, 2011, **13**, 17615-17624.
18. Z. Lei, N. Christov and X. S. Zhao, Energy & Environmental Science, 2011, **4**, 1866-1873.
19. J. Yan, T. Wei, B. Shao, F. Ma, Z. Fan, M. Zhang, C. Zheng, Y. Shang, W. Qian and F. Wei, Carbon, 2010, **48**, 1731-1737.
20. D. Wang, G. Fang, Q. Zheng, G. Geng and J. Ma, Journal of Solid State Electrochemistry, 2017, **21**, 563-571.
21. L. Deng, Z. Hao, J. Wang, G. Zhu, L. Kang, Z.-H. Liu, Z. Yang and Z. Wang, Electrochimica Acta, 2013, **89**, 191-198.
22. X. Cui, R. Lv, R. U. R. Sagar, C. Liu and Z. Zhang, Electrochimica Acta, 2015, **169**, 342-350.
23. X. Lu, H. Dou, B. Gao, C. Yuan, S. Yang, L. Hao, L. Shen and X. Zhang, Electrochimica

Acta, 2011, **56**, 5115-5121.
24. X. Mao, J. Xu, X. He, W. Yang, Y. Yang, L. Xu, Y. Zhao and Y. Zhou, Applied Surface Science, 2018, **435**, 1228-1236.
25. H.-C. Youn, S.-M. Bak, S.-H. Park, S.-B. Yoon, K. C. Roh and K.-B. Kim, Metals and Materials International, 2014, **20**, 975-981.
26. J. L. Gunjakar, A. I. Inamdar, B. Hou, S. Cha, S. M. Pawar, A. A. Abu Talha, H. S. Chavan, J. Kim, S. Cho, S. Lee, Y. Jo, H. Kim and H. Im, Nanoscale, 2018, **10**, 8953-8961.
27. J. L. Gunjakar, B. Hou, A. I. Inamdar, S. M. Pawar, A. T. A. Ahmed, H. S. Chavan, J. Kim, S. Cho, S. Lee, Y. Jo, S.-J. Hwang, T. G. Kim, S. Cha, H. Kim and H. Im, Small, 2018, **14**, 1703481.
28. Q. Pan, Y. Lv, G. R. Williams, L. Tao, H. Yang, H. Li and L. Zhu, Carbohydrate Polymers, 2016, **151**, 812-820.
29. G. Liao, S. Chen, X. Quan, H. Yu and H. Zhao, Journal of Materials Chemistry, 2012, **22**, 2721-2726.
30. N. He, O. Yildiz, Q. Pan, J. Zhu, X. Zhang, P. D. Bradford and W. Gao, Journal of Power Sources, 2017, **343**, 492-501.
31. Q. Zhou, J. Gao, C. Li, J. Chen and G. Shi, Journal of Materials Chemistry A, 2013, **1**, 9196-9201.
32. I.-Y. Jeon, Y.-R. Shin, G.-J. Sohn, H.-J. Choi, S.-Y. Bae, J. Mahmood, S.-M. Jung, J.-M. Seo, M.-J. Kim, D. Wook Chang, L. Dai and J.-B. Baek, Proceedings of the National Academy of Sciences, 2012, **109**, 5588-5593.
33. A. C. Ferrari, J. C. Meyer, V. Scardaci, C. Casiraghi, M. Lazzeri, F. Mauri, S. Piscanec, D. Jiang, K. S. Novoselov, S. Roth and A. K. Geim, Physical Review Letters, 2006, **97**, 187401.
34. A. C. Ferrari, Solid State Communications, 2007, **143**, 47-57.
35. R. Saito, M. Hofmann, G. Dresselhaus, A. Jorio and M. S. Dresselhaus, Advances in Physics, 2011, **60**, 413-550.
36. D. R. Dreyer, S. Park, C. W. Bielawski and R. S. Ruoff, Chemical Society Reviews, 2010, **39**, 228-240.
37. F. A. Gutierrez, J. M. Gonzalez-Dominguez, A. Ansón-Casaos, J. Hernández-Ferrer, M. D. Rubianes, M. T. Martínez and G. Rivas, Sensors and Actuators B: Chemical, 2017, **249**, 506-514.
38. P. L. Taberna, P. Simon and J. F. Fauvarque Journal of The Electrochemical Society, 2003, **150**, A292-A300.
39. Z. Chen, V. Augustyn, J. Wen, Y. Zhang, M. Shen, B. Dunn and Y. Lu, Advanced Materials, 2011, **23**, 791-795.
40. D.-W. Wang, F. Li, M. Liu, G. Q. Lu and H.-M. Cheng, Angewandte Chemie International Edition, 2008, **47**, 373-376.
41. J. Zhang, J. Jiang, H. Li and X. S. Zhao, Energy & Environmental Science, 2011, **4**, 4009-4015.

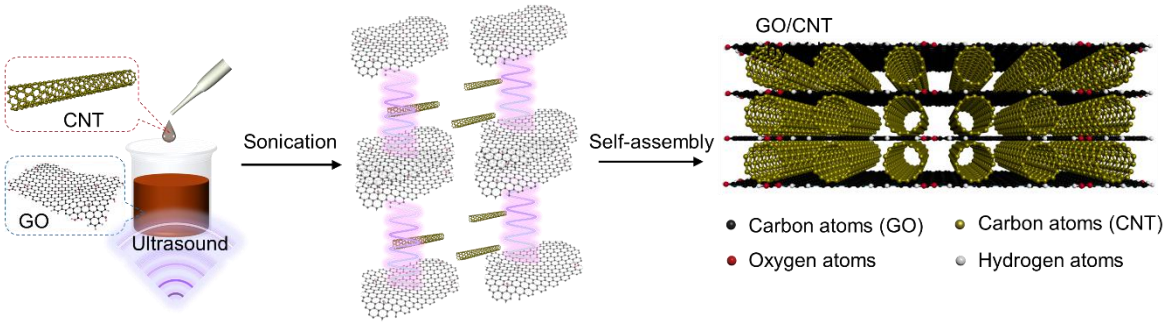

Scheme 1. A reaction scheme of the overall ultrasonication and self-assembly process for synthesis GO/CNT hybrids.

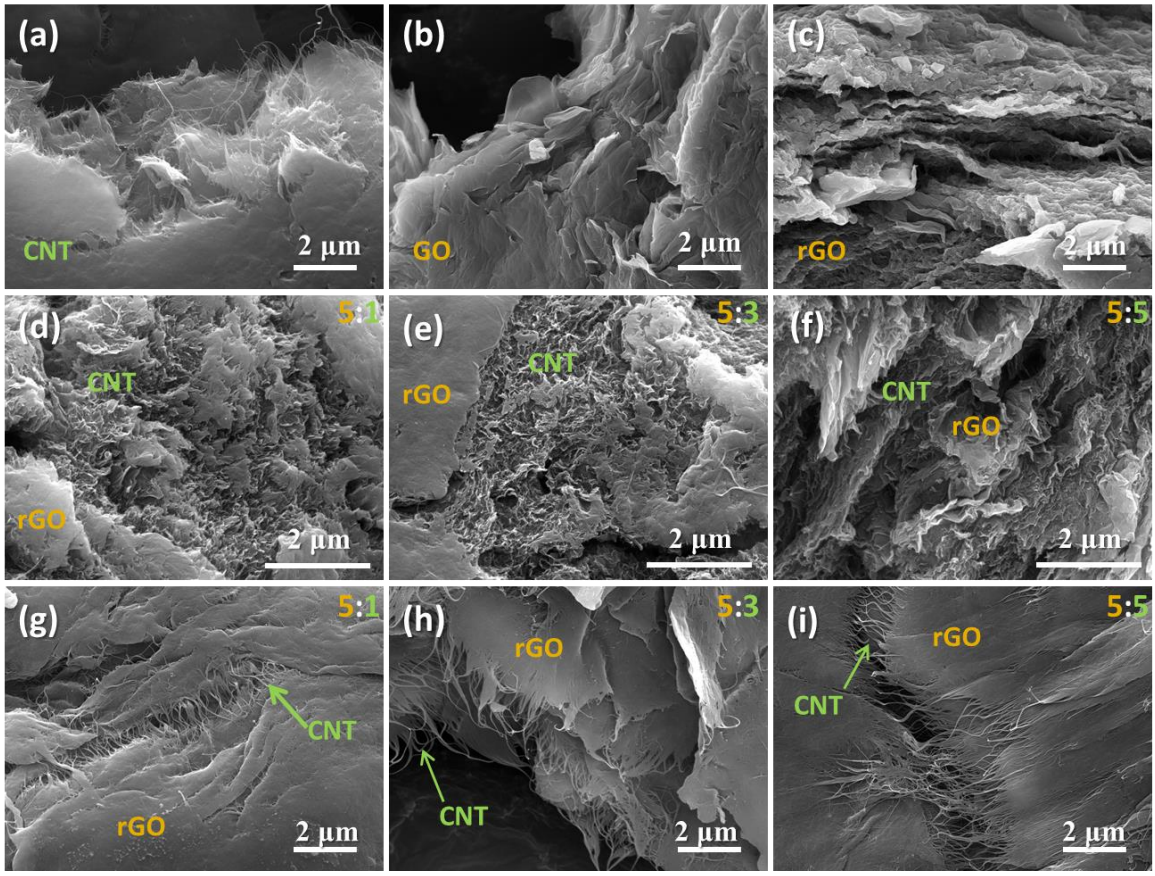

Figure 1. SEM images of (a) Ox-CNT, (b) GO, (c) rGO, (d, e, f) cross-section of rGO/CNT with different mass ratio of GC5:1, GC5:3, and GC5:5, respectively, and (g, h, i) top-section of rGO/CNT with different mass ratio of GC5:1, GC5:3 and GC5:5, respectively.

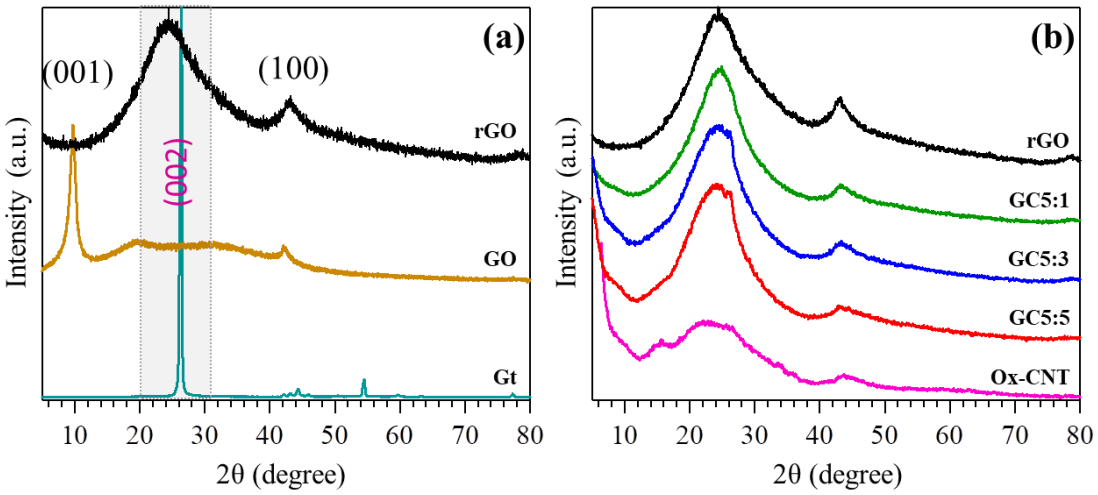

Figure 2. XRD spectra of Gt, GO, rGO (a), Ox-CNT, and rGO/Ox-CNT hybrids with a different mass ratio of 5:1, 5:3, 5:5 (b).

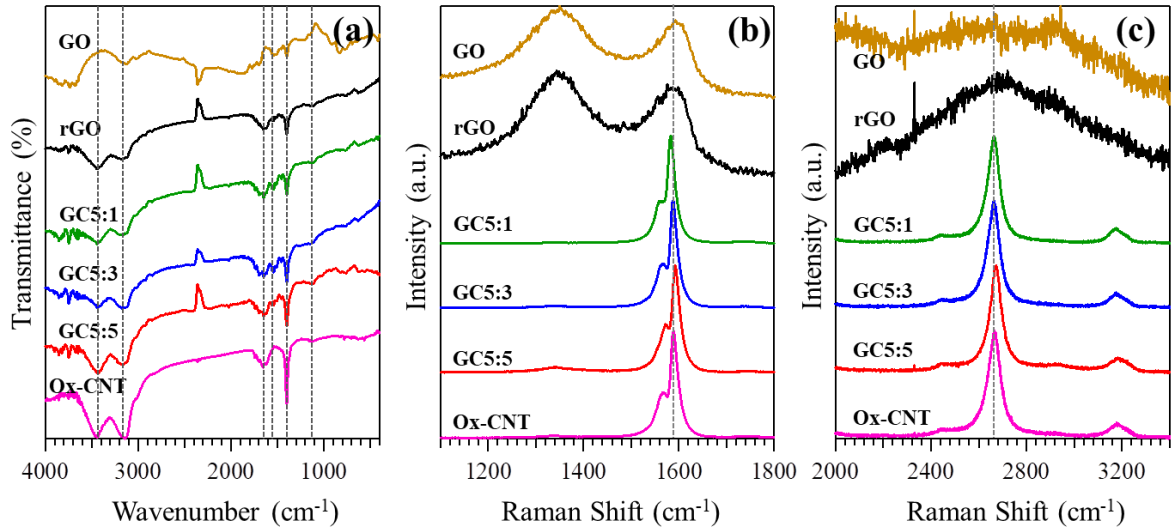

Figure 3. FT-IR (a) and Raman spectra (b, c) of GO, rGO, Ox-CNT, and rGO/Ox-CNT hybrids with different mass ratio of 5:1, 5:3, 5:5, (b) D-band and G-band region, (c) the expanded spectra at 2D-band and 2G-band region.

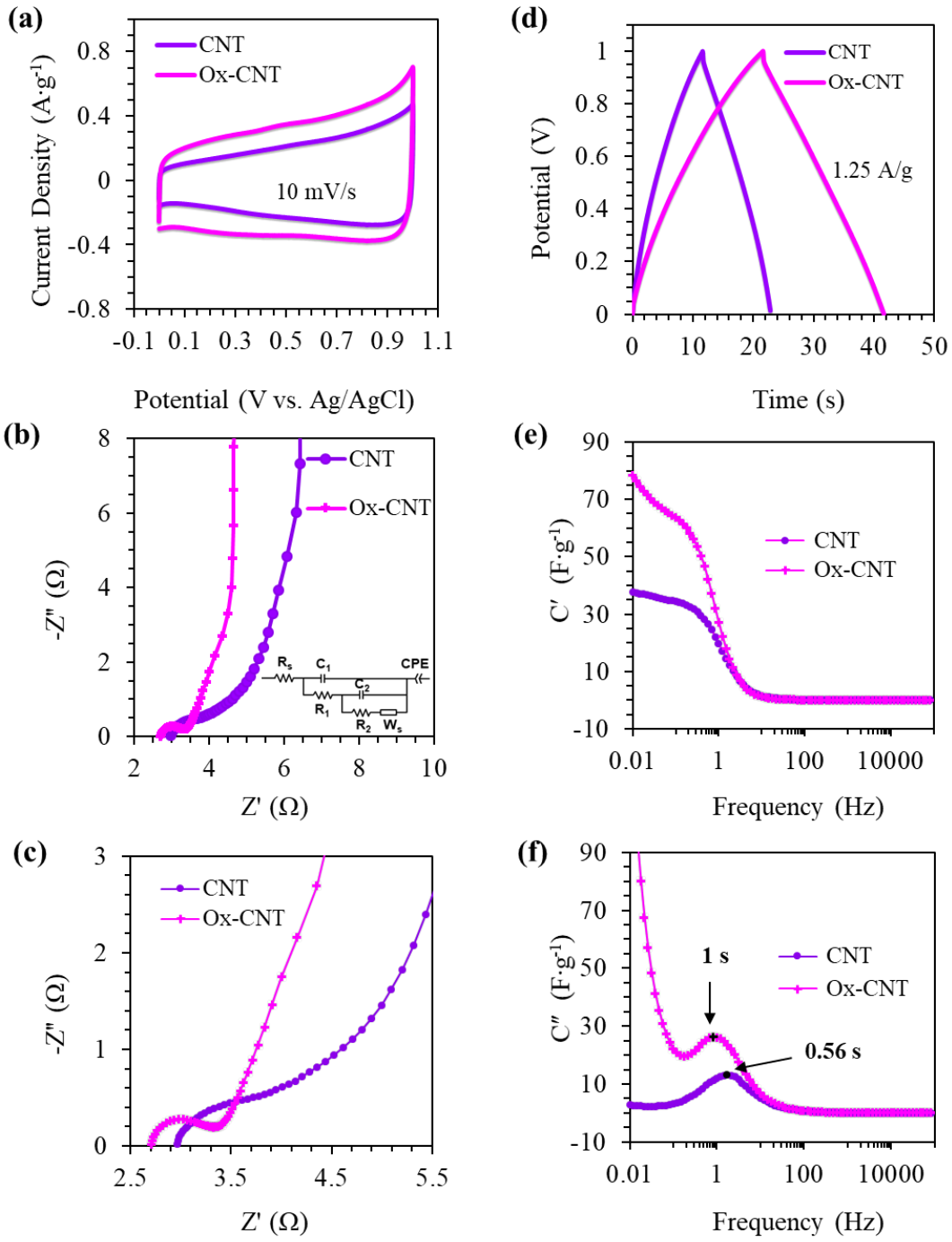

Figure 4. Electrochemical capacitance performance of CNT and Ox-CNT based supercapacitors. (a) CV curves at a scan rate of 10 $mV \cdot s^{-1}$, (b, c) Nyquist plots，(d) GCD curves at a current of 5mA, (e, f) Bode phase plots at a frequency range of 10^{-2}-10^{5} Hz.

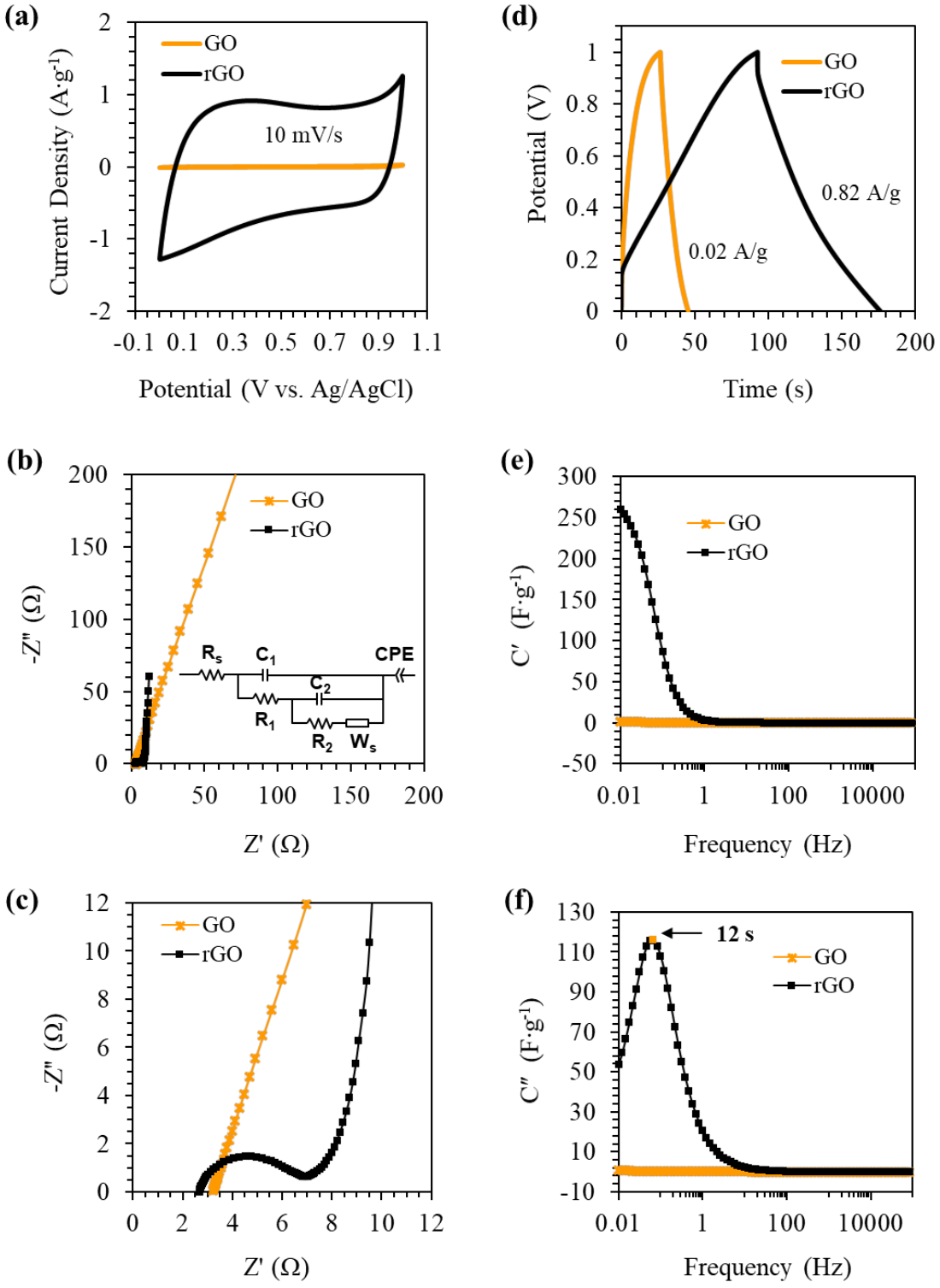

Figure 5. Supercapacitor application of GO and rGO. (a) CV curves at a scan rate of 10 $mV \cdot s^{-1}$, (b, c) Nyquist plots, (d) GCD curves at a current of 5mA, (e, f) Bode phase plots at a frequency range of 10^{-2}-10^{5} Hz.

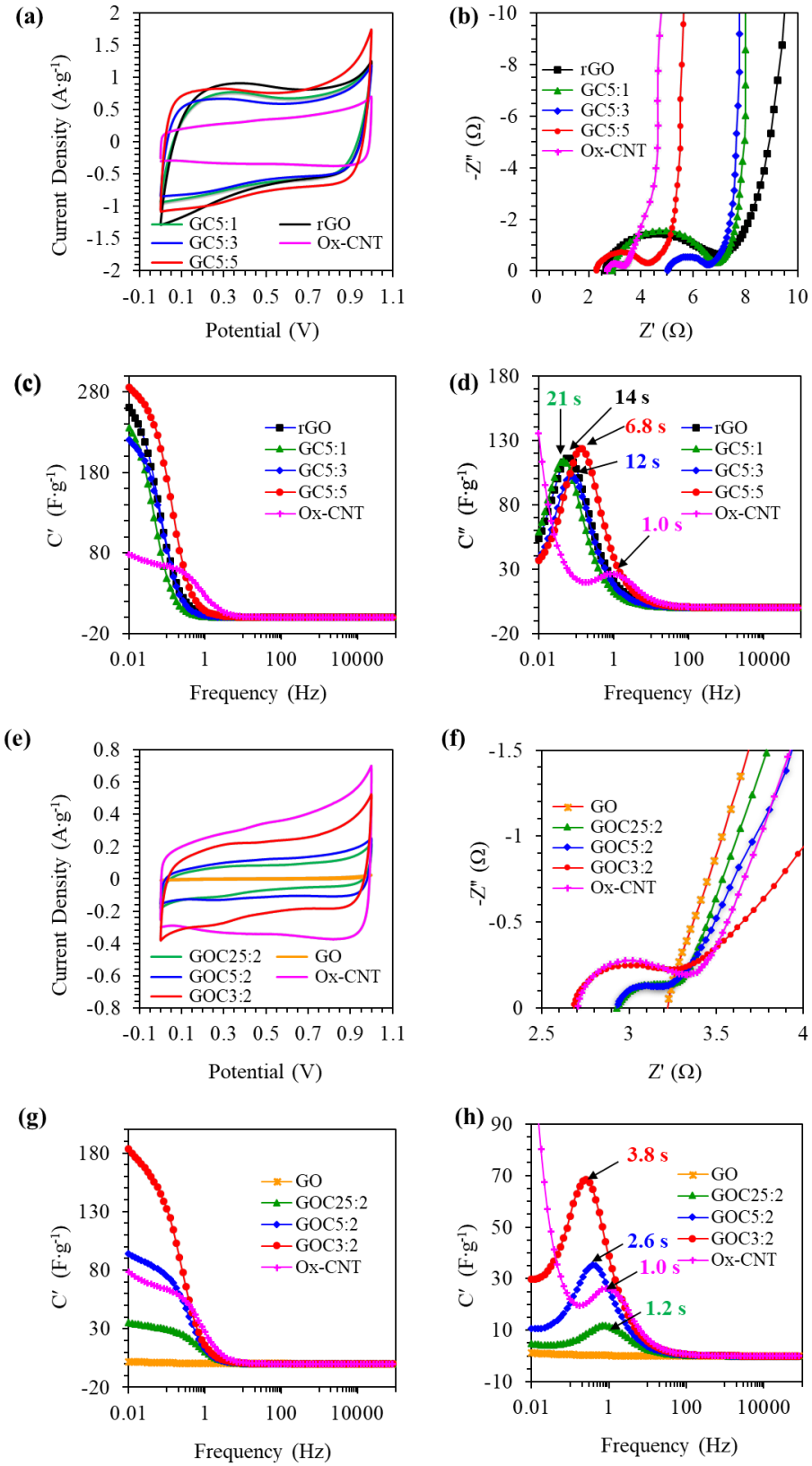

Figure 6. Electrochemical charge and ion transfer and storage performance in hybridised GO, rGO and Ox-CNT composites. (a, e) CV curves at a scan rate of 10 $mV \cdot s^{-1}$, (b, f) Nyquist plots, Bode plots of (c, g) real capacitance C″ vs Frequency and (d, h) imaginary capacitance C′ vs Frequency.

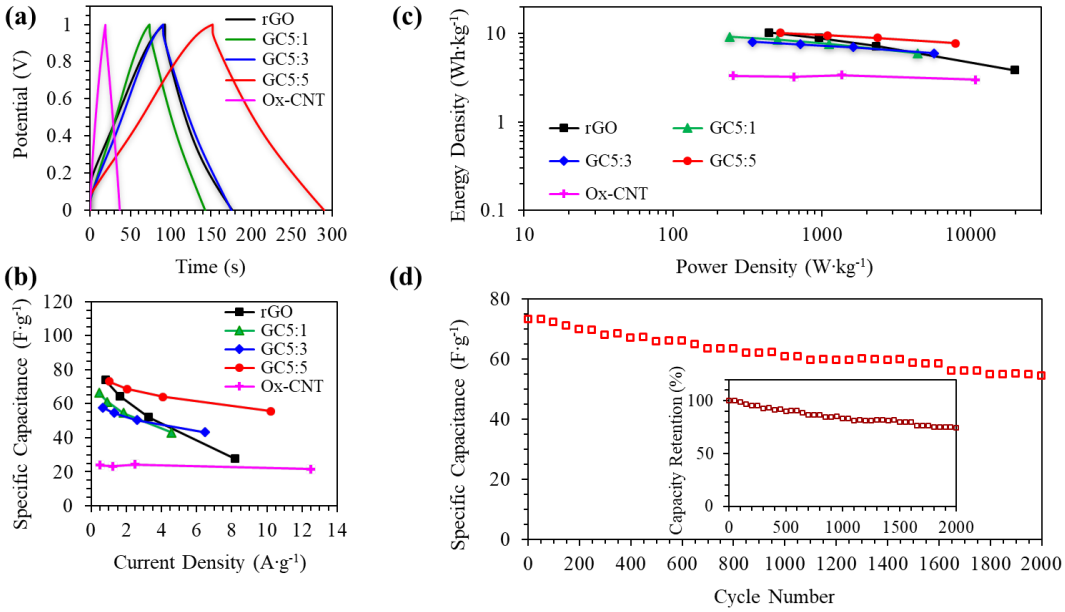

Figure 7. Rationalised supercapacitor performance of rGO/Ox-CNT hybrid with different mixing ratio. (a) GCD curves at a current of 5 mA, (b) specific capacitance. (c) Energy density vs power density. (d) The cycling stability of the GC5:5 electrode. The inset image shows capacity retention after 2000 cycles.

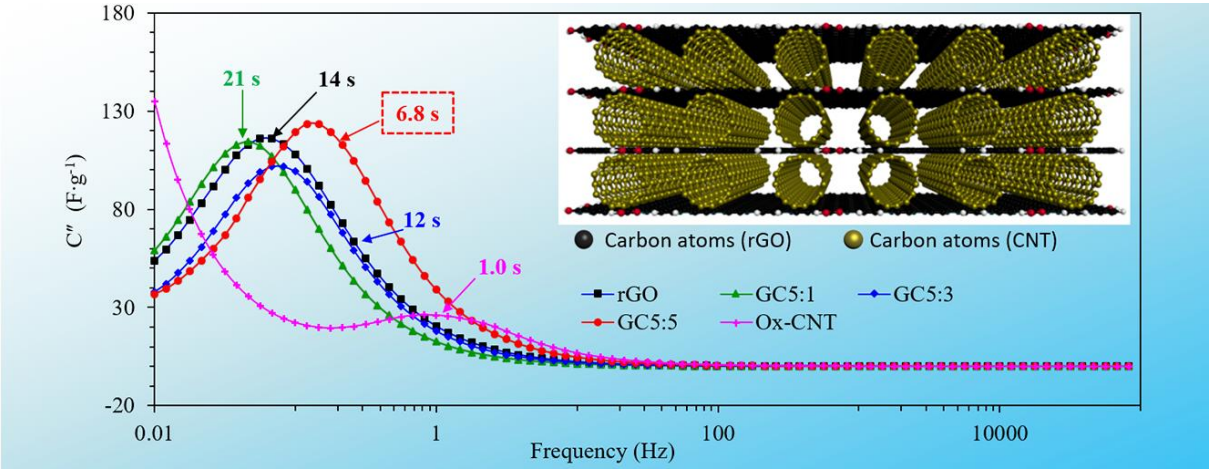

Table of Content